

Characterization of nanometric thin films with far-field light

Adi Salomon (✉ adi.salomon@biu.ac.il)

Bar Ilan University

hodaya Ester klimovsky

Institute of Nanotechnology and Advanced Materials (BINA), Bar-Ilan University, Ramat-Gan, Israel;
Department of Chemistry, Bar-Ilan University, Ramat-Gan, Israel

Omer Shavit

Bar Ilan University

Carine Julien

Université Paris Cité, CNRS, Saints Pères Paris Institute for the Neurosciences, F-75006 Paris.; Université Paris Saclay, Ecole Normale Supérieure Paris-Saclay, CNRS

Ilya Olevsko

Institute of Nanotechnology and Advanced Materials (BINA); Department of Chemistry, Bar-Ilan University, Ramat-Gan, Israel

Mohamed Hamode

Institute of Nanotechnology and Advanced Materials (BINA); Department of Chemistry, Bar-Ilan University, Ramat-Gan, Israel

Yossi Abulafia

Bar-Ilan Institute for Nanotechnology & Advanced Materials

Hervé Suaudeau

Université Paris Cité, CNRS, Saints Pères Paris Institute for the Neurosciences, F-75006 Paris, France.

Vincent Armand

Université Paris Cité, CNRS, Saints Pères Paris Institute for the Neurosciences, F-75006 Paris, France.

Martin Oheim

CNRS <https://orcid.org/0000-0001-8139-167X>

Article

Keywords:

Posted Date: October 27th, 2022

DOI: <https://doi.org/10.21203/rs.3.rs-2077356/v1>

License:  This work is licensed under a Creative Commons Attribution 4.0 International License.

[Read Full License](#)

Abstract

The fabrication and characterisation of ultra-thin, transparent films is paramount for protective layers on semiconductors, solar cells, as well as for nano-composite materials and optical coatings. Similarly, the probe volume of nano-sensors, as well the calibration of axial distances in super-resolution microscopies, all require the metrology of axial fluorophore distances. However, the reliable production and precise characterisation of such nanometric thin layers are difficult and labor-intensive and they require specialized equipment and trained personnel. In our present work, we describe a simple, non-invasive, all-optical technique for simultaneously measuring the refractive index, thickness, and homogeneity of such thin films. We assemble transparent layers from My-133-MC, a biomimetic transparent polymer with a refractive index of 1.33, amenable for applications in the life sciences. All parameters characterising the films are obtained in a single measurement from the analysis of supercritical angle fluorescence radiation patterns acquired on a minimally modified inverted microscope. Results compare favorably to those obtained through a combination of atomic force and electron microscopy, surface-plasmon resonance spectroscopy and ellipsometry. To illustrate the utility of our technique, we present two applications, one in metrology and one in bio-imaging; (i), the calibration of axial fluorophore distance in a total internal reflection fluorescence geometry; and, (ii), live-cell super-resolution imaging of organelle dynamics in cortical astrocytes, an important type of brain cell. Our approach is cheap, versatile and it has obvious applications in profilometry, biophotonics, photonic devices, and optical nano-metrology.

Introduction

Thin films are essential building blocks for optical coatings, organic/inorganic¹ or photonic devices^{2,3}, nano composites^{4,5}, as well as transparent nano- and micro-structures^{6,7}. Ultra-thin polymer films also play crucial roles as transparent microwells⁶, or as scaffolds in nanofluidics^{1,2}. Considerable efforts are devoted to the characterisation and metrology of such thin films and 2-D materials, typically requiring complicated, expensive and time-consuming techniques, such as ellipsometry, stylus profilometry, atomic force microscopy (AFM), scanning electron microscopy (SEM) and others, which require clean-room facilities and specialized personnel. Here, we show that much of the same information can be retrieved from a single, all-optical measurement, on a standard inverted microscope, equipped with a high-numerical aperture (NA) objective. We achieve this measurement by first depositing a thin fluorophore layer on top of the transparent nanometric film to be characterized and then imaging the fluorescence radiation pattern by aid of a phase telescope (Bertrand lens). The latter shifts the image plane from the usual front focal plane, (sample plane, SP), to the objective's back focal plane (BFP). The BFP image contains the k-space representation of the emission from all fluorophores in the illuminated area. It provides directional information that is otherwise lost^{8,9}, and it allows us monitoring subtle changes in the fluorophore radiation pattern in real time.

Our technique is based on the analysis of supercritical angle fluorescence (SAF) emission of fluorophores located very close to the interface. The radiation pattern of near-interface fluorophores is different from

that of the classical dipole emission in free space^{10,11}. We here exploit that this pattern is further modified, not only by changes in the proximity of the fluorophores to the interface, but also by the local RI and the homogeneity of the transparent film: while the precise position of the intensity maximum at the emission critical angle θ_c provides a sensitive measurement of the RI of the medium in contact with the fluorophores^{12,13}, the relative intensity emitted into supercritical- vs. under-critical angles encodes the fluorophore distance from the interface¹⁴⁻¹⁶. Our technique does not require any specialised equipment other than an objective satisfying Abbe's sine condition; by collecting information from the extreme periphery of a high-NA objective's back pupil, we retrieve - in the far-field - information originating from the dipoles' near-field and its interaction with the interface.

Our paper is organised as follows: We first describe the fabrication of a set of test samples in which a 5-nm thin homogenous fluorophore layer is sandwiched between transparent spacer and capping layers of My-133-MC polymer. We produced an otherwise identical sample series with precisely controlled fluorophore heights (film thicknesses) from 10 to 340 nm. We then acquire and analysed BFP images to confirm the RI of 1.33 - mimicking a cell environment for later biological applications - and quantify the fluorophore height and homogeneity of the produced samples. We held these SAF-based results against data obtained with classical nano-characterization techniques. In the third part of our paper we provide two examples of applications, one in optical nano-metrology, and the other one in biological time-lapse imaging of organelle dynamics. The here presented approach is easy to implement and it presents a significant advance over existing techniques, in terms of speed, cost and ease. We expect it to become a routine step in thin-film and 2-D material characterization, and a complement to evanescent-wave¹⁷ and other axial super-resolution techniques¹⁸, where it can considerably enlarge the information content compared to that of fluorescence-intensity images alone.

Results And Discussion

Controlled fabrication of ultra-thin polymer films having a refractive index close to water

My-133-MC is a commercial, transparent polymer having a RI of 1.33, similar to that of the aqueous environment of the cytosol of a biological cell¹⁷. My-133-MC cures upon exposure to ambient moisture. Using this polymer, we assembled transparent layered structures through a combination of spin-coating and plasma surface-activation techniques. Figure 1a shows a typical cross-sectional image, illustrating the nano-layered architecture of the resulting sandwiches. They exhibit, from bottom to top, a borosilicate substrate (BK-7 optical-grade coverslip), a flat My-133-MC spacer layer of controlled nm-thickness; a 5-nm thin fluorescent-emitter layer and, on top, another transparent index-matched polymer-capping layer. This μm -thick capping layer ensures that the dye molecules are exposed to a homogenous RI microenvironment. In the particular sandwich shown, we deposited additional conductive layers at the very bottom and on top, only for the purpose of electron microscopy. On the focused-ion beam (FIB)

cross-section (left), we observe a remarkable homogeneity, smoothness and flatness of the different component layers (see also **Fig. S1** in the **Supplementary Material Online**).

As an emitter we used a well-characterized far-red emitting porphyrin derivative, (H6TPPS) J-aggregate. In addition to the large Stokes' shift, advantages of TPPS are its water-solubility, resistance against photobleaching and high absorption cross-section¹⁹. TPPS aggregates retained their bulk fluorescence properties when sandwiched between the polymer layers, with neither a change in peak absorption (S2 at 491 nm, and S1 at 700 nm) nor in peak fluorescence (720 nm), Fig. 1b. From the measured optical densities, we estimate an equivalent dye concentration of $\sim 0.1\text{M}$ within the nm-layer. We obtained large uniform dye coverage onto surfaces up to several mm^2 , Fig. 1c. Dye was either deposited on the bare surface or on an intermediate spacer layer of My-133-MC polymer. Spin coating allowed us to form a homogenous polymer spacer layer and to systematically control its thickness by varying the angular frequency and polymer concentration, Fig. 1d. We used stylus profilometry and AFM for measuring the resulting layer thickness, Δ , Fig. 1e. The obtained layers had heights Δ of a few to hundreds of nm and a RMS roughness (R_q) of the order of 1–2 nm, independent of Δ . Ellipsometry confirmed a RI of about 1.33, as specified for My-133-MC polymer, Fig. 1f.

Taken together, through a combination of nano-fabrication and -characterization techniques we assembled and experimentally confirmed smooth, flat and uniform nano-layered structures alternating transparent and fluorescent layers. With their transparency and RI close to that of a biological cell, they feature a thin, uniform and sufficiently bright dye layer, at a precisely controlled distance from the glass substrate's surface. Such sandwiches can serve, e.g., as a calibration tool for various axial super-resolution microscopies^{15,20}, as shown later. Our samples also have applications in nanotechnology, material science, molecular plasmonics, physics and nanobiology.

Thin-layer refractometry using far-field light

A dipole's radiation pattern changes when the emitter approaches an interface. Next to the boundary, the evanescent (near-field) emission component can couple to the interface and become propagative. By analogy to the excitation evanescent field in TIRF that requires supercritical illumination angles, this covered near-surface emission must propagate at supercritical angles, forbidden by Snell's law for far-field emission. In fact, near-interface fluorophores emit an important power fraction into the higher-index medium (n_2), and more and more beyond the emission critical angle $\vartheta_c = \text{asin}(n_1/n_2)$ the closer the fluorophore is to the surface. When imaged with a sufficiently high-NA objective, this supercritical angle fluorescence (SAF) is seen (for isotropic emitters) as a bright ring on BFP images, and ϑ_c marks the emission intensity transition between under- (darker) and supercritical (brighter) zones. The RI of the local environment of the fluorophores is then obtained as $n_1 = f/rc$, where rc is the equivalent critical radius and f the focal length of the objective, Fig. 2^{12,13}.

We implemented toggled SP and BFP imaging on an inverted objective-type total internal reflection fluorescence (TIRF) microscope built from optical bench components (**Fig. S2**). Our instrument allows for

the continuous selection of the polar illumination angle at the sample, between $\vartheta=0^\circ$ (epifluorescence, EPI) and $\pm 74^\circ$ (TIRF). We limited the scan angle to this value so as not to clip the laser beam by the objective, having a measured^{13,21} effective NA_{eff} of 1.465 ($\sim 75.7^\circ$). Before each experiment, we systematically ran a test protocol validating the alignment, setup performance and the absence of coverslip tilt (**Fig. S3**).

We then turned to our nano layered sandwiches, focussing at the dye layer using a piezo-electric focus device. Emission from the 5-nm thin TPPS J-aggregate layer was bright enough for recording contrasted BFP images on a standard back-illuminated sCMOS camera with reasonable acquisition settings ($P = 40 \mu\text{W}$ at the objective and 100-ms integration time), Fig. 2a. The recorded BFP images showed radially symmetry, indicative of non-preferentially oriented dipoles. They also showed the expected characteristic intensity transition at the emission critical angle ϑ_c with an intensity maximum just above ϑ_c , and an outer boundary at NA_{eff}. Line profile intensities, but neither peak positions nor the measured RI values, were sensitive to coverslip tilt further confirming the robustness of our measurement (**Fig. S4**). The deposit of a My-133-MC polymer capping layer on top of a dye-coated BK-7 substrate ($\Delta = 0 \text{ nm}$), modified the measured BFP pattern and measure RI from 1.047 ± 0.002 (air) to 1.3182 ± 0.003 (My-133-MC), Fig. 2b (see panel c for a polar-plot representation as radiation patterns). The measured RIs were independent of the azimuthal orientation of the very line profile chosen (panel b). As a consequence, our SAF-based RI measurements were highly reproducible and consistent for many independent samples, Fig. 2d.

Ultra-thin polymer layers have homogenous RI over hundred μm

SAF-based refractometry is precise, but it only probes a small surface area delimited by the illuminated spot size. To characterize the produced layers over larger spatial scales we turned to nanoplasmonics. Surface plasmons are evanescent waves that strongly depend on the dielectric function of the medium in contact. To avoid tedious phase-matching and couple free propagating light to plasmonic modes, we employed plasmonic nanostructures that scatter the incoming light and thereby overcome the k-vector mismatch by additional momentum from the reciprocal lattice. We milled periodic nano-hole arrays into a thin Au-film deposited on the same BK-7 glass substrate as used before. We observed on a dark-field microscope structural colors that varied among plasmonic hole arrays according to their periodicities, P , i.e., inter-hole spacing (340, 380 and 420 nm)^{10,20,22} Fig. 3c shows typical transmission spectra obtained from those arrays upon white-light illumination. Identical peaks are observed for plasmonic structures covered with either water or My-133-MC polymer, validating the same RI for both. These measurements probed length scales over a $> 100 \mu\text{m}$.

Taken together, our ellipsometric (Fig. 1f), SAF-derived (Fig. 2) and plasmonic RI measurements (Fig. 3) independently confirm a consistent RI of ultra-thin My-133-MC layers close to that of water, validating this transparent polymer as an optical medium for diverse biomimetic applications in microscopy and biophotonics.

Detecting imperfections of the polymer thin layers

MY-133-MC is quite a challenge to work with. Although we routinely filtered the polymer solution to remove air bubbles and obtain flawless, uniform and homogenous polymer films, BFP images sometimes revealed a conspicuous double-ring structure featuring two intensity transitions, one at RI = 1.33 and another one at RI = 1, Fig. 4a (*left*). The inner ring was dimmer compared to the outer one, and the diameter of the outer ring corresponded to that observed with the majority of produced polymer samples (*right* half-image).

We reasoned that such a double-ring pattern could result if some fluorophores were exposed to air rather than the polymer, due to, e.g., cavities, cracks or bubbles in the polymer (**Fig. S5**). A *post-hoc* FIB cross-section on samples showing a double-ring confirmed the presence of μm -sized bubbles, Fig. 4b. This size is probably an overestimate, given that SEM images were acquired in vacuum. Imperfections could equally be observed on the plasmonic hole arrays on which polymer layers were deposited, lending further plausibility to our interpretation (**Fig. S6**). Dual RIs could also result from cracks or dimples in the upper coating layer. Figure 4c shows such an example for which a marked RI change was observed upon wetting the polymer surface. Starting from an air-dominated environment, pipetting a drop of polymer onto the surface changed the BFP image from a double-ring structure – with the presence of an intensity transition at RI = 1 (image frame marked in *green*), to 1.3 (*blue*) - the change abruptly occurring at the very moment of the deposit of the drop (*red*). Thus, the information contained in the fluorophore radiation pattern does not only permit precise thin-layer refractometry but it also reveals imperfections, the detection of which requires otherwise more involved, lengthy and expensive experiments. Figure 4c illustrates that our technique permits *in operando* refractometry, an important feature for sensors and thin-film devices. Based on SAF-based BFP-image refractometry, we retained only samples that passed the quality gate of a single-ring BFP pattern, and we next investigated how changes in the thickness of the spacer layer, i.e., the fluorophore height above the substrate, affected the radiation pattern.

Measuring axial nanometric distances from SAF/UAF ratios

Capitalizing on our ability to fabricate homogeneous, thin polymer layers of controlled heights, Δ , we prepared a series of otherwise identical sandwiches featuring a TPPS emitter layer at $\Delta = 0, 5, 15, 25, 32, 29, 75$ and at 340 nm, respectively. Three of these samples are schematized on Fig. 5a. We excited TPPS fluorescence at 488 nm, using TIRF. The focused laser spot is seen twice in the periphery of the BFP image, marking the positions of the incoming and back-reflected beam, respectively, and allowing a direct calibration of the beam angle ϑ from the BFP image^{22,23}. As expected from the evanescent-wave decay in axial direction, the detected intensity dropped with increasing Δ , Fig. 5b. While the evanescent-wave penetration depth can be calculated from the local RI of the medium ($n_1 = 1.33$ for My-133-MC) and the incidence angle of the illuminating beam at the laser wavelength the actual depth in a given experiment, on the particular microscope is much less certain. How deep the excitation light actually penetrates into the sample is difficult to know and is modified by sample, surface and objective imperfections²⁰, which

make the interpretation of TIRF images in terms of axial fluorophore height from single-angle TIRF data problematic, and which - in the past - have called for multi-angle or normalization approaches²⁴.

The ratio of the integrated supercritical (SAF) vs. undercritical fluorescence (UAF) emission intensities, $R = I_{SAF}/I_{UAF}$, is a sensitive function of fluorophore height Δ , Fig. 5c. Because the light passing through the supercritical zone of the BFP can only originate from the fluorophore near field, the farther away from the interface the fluorophore resides, the dimmer will be the SAF component^{25,26}. UAF on the other hand, is almost constant, with the exception of a small surface effect very close to the interface¹⁶.

Advantageously, the SAF/UAF fluorescence ratio normalizes for variations in fluorophore concentration, bleaching, fluctuations in laser intensity and other factors that linearly influence the measured signal. We segmented background-subtracted BFP images into undercritical and supercritical regions, based on the previously measured NA_{eff} and RI and integrated the intensities over these regions. Figure 5c graphs the evolution with Δ of the SAF/UAF ratio $R = I_{SAF}/I_{UAF}$, along with simulations for different fluorophore orientations, based on the constant total-radiated power model from Hellen & Axelrod²⁷. We see a good agreement with theory, except for values very close ($\Delta < 15$ nm) to the interface, where the observed ratios were lower than the predicted ones.

While we can exclude systematic errors in the thickness of the spacer layers from our earlier electron-microscopy controls, one possible explanation is that surface quenching affects SAF stronger than UAF, or that fluorophore orientation is modified in a surface-distance dependent manner, e.g., by surface charges. Alternatively, the objective might not be as efficient in capturing very high-angle emission (SAF) as capturing lower-angle (UAF) light. In fact, theory assumes a flat collection efficiency over the entire solid angle covered by the NA, which might not be the case for the used objective lens. Might that as it be, a systematically lower fractional SAF would also explain why the best fit (*grey* thick trace) corresponds to theory (*blue* dash), up to a constant scaling factor (x0.86). Another reason for this offset could be a generally higher UAF fraction than expected: for example, if My-133-MC polymer was even slightly autofluorescent, this would produce a relatively higher UAF signal (resulting from the spacer and capping layers) and be detectable under the low-background conditions of the TIRF experiment. Yet, we could not detect any detectable autofluorescence on a fluorescence spectrometer (not shown). Of course, the objective itself or the immersion oil could fluoresce and contribute UAF, although we sought to minimize such effects by the detection in a fluorescence band of (720 ± 30) nm, centered on TPPS.

Taken together, even with the note of caution for $\Delta < 15$ nm, SAF/UAF ratiometry allowed us a reliable, quantitative analysis of the thickness of ultra-thin layers in the sub-100-nm range, with a precision and accuracy higher than that of typical TIRF-intensity based z-measurements.

Imaging single-organelle dynamics in live cells using SAF/UAF emission ratios

One example of biological axial nanoscopy that would benefit from a preciser axial fluorophore localization is the analysis of single-vesicle mobility during regulated exocytosis, which was pioneered in

TIRF studies during the late 1990^{28–30} and is widely been used in the cell- and neurobiology community. Exocytosis, release of substances from the cell, involves the transport, docking and emptying into the extracellular space of tiny, membrane-delimited and cargo-loaden compartments ('vesicles') that are formed and filled inside the cell, actively transported to the cell's outer membrane and that, upon a stimulus - often a rise in the intracellular free calcium concentration ($[Ca^{2+}]_i$), fuse with the outer membrane to release their contents, see Fig. 6a. In such experiments, it would be important to know if a vesicle is close to the membrane or just a bit above, if it moves towards it or away from it, or if it simply loses fluorescent content by dye leakage or photobleaching - questions that cannot be easily answered from a single-angle intensity TIRF recoding, due to the unknown evanescent-wave penetration depth and the confounding effects of dye concentration and fluorophore distance on single-vesicle brightness. Unfortunately, the fast dynamics of exocytosis does neither permit capturing z-stacks of images for axial localization at higher precision, nor acquiring a variable-angle series of TIRF images for a 'tomographic' reconstruction of vesicle localization.

We studied, in cultured mouse cortical astrocytes labelled with an amphiphilic styryl pyridinium dye³¹, the radiation pattern emerging from small regions of evanescent-wave illuminated membrane, close to the coverslip. In astrocytes, a glial type of brain cells that are neighbors to most neuronal synapses, the green-yellow emitting non-membrane permeable dyes FM1-43 or FM3-25³² show a behavior and uptake-mechanism different from that in neurons and are internalized to label larger vesicular compartments, called lysosomes³¹. On EPI images these lysosomes appear as diffraction-limited bright fluorescent spots in front of a diffuse background resulting from a faint cytoplasmic staining, Fig. 6b. On a time-lapse series of TIRF images we can appreciate the movement of some lysosomes in and out of the thin layer illuminated by the evanescent field, while others dwell patiently close to the plasma membrane, Fig. 6c. Stimulation of exocytosis by application of extracellular adenosine triphosphate (ATP) activates purinergic receptors and increases $[Ca^{2+}]_i$, leading to a loss of most near-membrane lysosomes docked at the basal plasma membrane, leaving only 1–2 spots in the imaged area, Fig. 6d. This interpretation is confirmed by analysing BFP images that were taken alternately with SP images and that reproducibly displayed R values of 0.59–0.63 (0.56 ± 0.05 , $n = 15$) for cells with neither exocytic events nor overt mobility. Following the loss of near-membrane lysosomes, the measured SAF/UAF ratios were consistently lower, $R = 0.36 \pm 0.06$, explained by an average localization of the remaining dye molecules slightly deeper within the cell, more distant from the interface. Clearly, the FM dye molecules on those organelles are less capable of emitting SAF. The interest of concurrent sample- and pupil-plane analysis is evident from the rightmost panel for which R was 0.30 ± 0.02 , despite the fact that a single lysosome was still present on the sample-plane image. While pure TIRF intensometry would suggest a membrane-proximal location, SAF/UAF ratiometry revealed a R value explained only by a greater distance of the fluorophores from the basal cell membrane than suggest from the TIRF intensity reading alone. SAF/UAF ratiometry can thus eliminate unknowns like dye concentration, vesicle diameter or local illumination heterogeneities³³ and permit a more reliable interpretation of near-membrane fluorescence dynamics.

By comparison with the ratios measured for our thin films (Fig. 5c) we can infer that lysosomal dynamics occurs in near-membrane region closer than 100 nm to the coverglass. SAF/UAF ratiometry, similar to TIRF, thus allows the resolution of axial fluorophore dynamics within this range. One limitation of the R measurements in the current implementation of the microscope, however, is that they average fluorophore properties over the field-of-view (FOV, some 30 μm diagonal) and we are thus limited to cells with only a few labeled lysosomes in the FOV. More resolved measurements can be expected when reducing the size of the illuminated area, e.g., by using Bessel-beam illumination with an evanescent needle of light³⁴.

Our proof-of-concept biological experiments illustrate the usefulness of concurrent sample- and back-focal plane imaging for interpreting and disambiguating the dynamics of biological fluorescence, and they also illustrate the interest of fluorescence imaging with combined TIRF excitation and SAF detection^{11,35} in conjunction with a rapid, online BFP-image analysis. We expect our technique to have applications in various fields of “surface biology”, like the dynamics of ER-PM junctions that link the endoplasmic reticulum to the plasma membrane, cellular adhesion sites, or biofilm growth, but also in surface chemistry and material science.

Discussion

The combination of nano-fabrication and -characterization techniques allowed us to assemble and validate controlled, smooth and uniform sandwiches featuring nm-thin fluorescent transparent layers at precisely defined axial distance and embedded in an environment having a RI close to that of a biological cell. Our sandwich samples can serve, e.g., as a nanoscopic axial ruler for axial super-resolution microscopies, based on astigmatic^{36,37}, multi-focal^{38,39}, or defocused imaging^{40,41} but also on other point-spread-function engineering techniques^{42,43} and they provide a valuable reference for interpreting the axial dynamics of intracellular processes in the near-membrane space of live cells, cultured on a glass coverslip^{44,45}. We demonstrate that combined sample-plane and quantitative BFP imaging provides detailed insight into fluorophore properties and axial dynamics. SAF based refractometry and SAF/UAF ratioing can be used for exploring the physical and chemical microenvironment of fluorophores and can be used for time-lapse *in situ* imaging of fluorophore dynamics at or close to a dielectric interface.

BFP imaging is easily implemented on a standard inverted microscope and it allowed us to retrieve fluorophore information in the 20- to 100-nm range. The analysis of the fluorophore radiation pattern gives access, via a single measurement, to the RI of the fluorophore-embedding medium, the fluorophore height (or film thickness) and orientation of emitters, with the only condition that they are sufficiently close for their near-field and SAF emission component to be modulated by the surface proximity. As a simple and reliable far-field optical technique, the SAF-based fluorophore-height measurement is an interesting alternative and complement to other axial nanoscopies. For the sub-20-nm range where our technique lacks sensitivity, quenching-based optical rulers, based on plasmonics⁴⁵, distance-dependent

fluorescence-lifetime modulation⁴⁶, metal-induced energy transfer (MIET)⁴⁷⁻⁴⁹, or transparent conductive oxide (TCO-) based transparent rulers⁵⁰ can close the gap, offering nm sensitivity.

Conclusion

Our technique fits not only to biological super-resolution imaging, but also to of molecular plasmonics, or polaritons in chemistry, where the nanofabricated samples and the proposed k -space imaging technique together offer a powerful tool for studying strong coupling between emitters and plasmonic system^{20,22,37}. In fact, for the here described controlled nanolayers, the interaction between molecules and plasmons is very well defined, and so is the coupling (Rabi splitting) that is not averaged over emitters at different distances. Finally, we also expect our axial-nanoscopic rulers to become a standard for various areas of nano-metrology⁵⁷. With their transparency and RI close to that of a biological cell, our transparent fluorescent sandwich samples alone feature a thin, homogenous and uniform dye layer, at a precisely controlled distance from the glass substrate's surface and can be used as calibration standards for axial optical sectioning, super-resolution and fluorophore localisation techniques. The SAF/UAF ratios that can be reproducibly obtained from our test samples can instruct axial measurements from unknown samples, e.g., to disambiguate biological recordings from TIRF or other near-field or axial super-resolution microscopes that have been challenging to validate.

Materials And Methods

Materials. We chose My-133-MC (MyPolymers LTD, Ness Ziona, Israel) for its RI close to that of water and two fluorinated (Hydro-Fluoro-Ether, HFE) compounds as solvents for this polymer, Novec™ 7500 or 7100 (3M™, Minnesota, USA). For the fluorescent emitter layer, we opted for H₆TPPS₄ (meso-tetra 4-sulfonatophenyl porphyrin) (Sigma-Aldrich, #88074) in its J-aggregate form due to its far-red/near-IR emission remote from autofluorescence and most biological fluorophores (peak absorption/emission wavelength, $\lambda_{\text{abs}}/\lambda_{\text{em}} = 488/720 \text{ nm}^{21}$).

Thin-film polymer deposition. #1 BK-7 glass coverslips (Menzel Gläser, Braunschweig, Germany) were cleaned in 1/100 Hellmanex/double-distilled-deionized water (DI water, 18.2 mΩ) and sonicated (20 min, 40°C). They were then rinsed thoroughly with DI water, ethanol, and DI water again (30 s each). Substrates were dried with a N₂ flow and immediately used thereafter. MY-133-MC polymer solution was filtered and thin films were spin-coated (WS-650, Laurell Tech Corp., North Wales, PA) and cured under ambient conditions (RT, 20–22°C) during at least 6 hours. My-133-MC polymer resin was applied either pure (undiluted) or diluted in HFE-7500.

Thin dye-layer deposition. H₆TPPS₄ was dissolved in DI water and aqueous nitric acid (65% w/w, Sigma-Aldrich) to reach pH ~ 1. The thin film-deposition procedure is described elsewhere²¹. Absorption and fluorescence spectra were recorded both from films and in solution, using a home-built microspectrofluorimeter built around an Olympus inverted microscope coupled to a spectrophotometer

(IsoPlane SCT-320, Princeton Instruments, Trenton, NJ) and equipped with a charge-coupled device camera (CCD, PIXS1024b, Princeton Instruments).

Nanoplasmonics. Plasmonic structures were milled in our in-house clean rooms, using a Gallium focused-ion beam (Helios NanoLabDualBeam 600, FEI Electron Optics, Eindhoven, The Netherlands) into previously deposited 200-nm silver films. The fabrication process was entirely calibrated for milling depth, beam size, and beam deflection. The integrated scanning electron microscope (SEM) enabled the *in-operando* imaging of the fabricated structures as shown.

Thin-film characterization. Film thickness and roughness were measured using a Stylus Profiler (DektakXT, Bruker) in at least 6 different areas. RMS surface roughness (R_q) was calculated using Mountains8 (Digital Surf). Results were cross-validated on the same specimens with AFM (Nanoscope, Veeco). The AFM images are shown as pseudo-colored height maps, from which R_q was calculated. RIs were measured by spectroscopic ellipsometry (J.A. Woollam, M-2000), nanoplasmonics and SAF (see below). For ellipsometry, we constructed a model for the My-133-MC polymer, based on the known wavelength and thickness of the deposited layers, obtained by SEM (See **Fig. S1**).

Combined TIR-SAF imaging. Fluorescence imaging was performed on a custom inverted microscope assembled from optical bench components (see **Fig. S2** for details). Briefly, the beam of a 488-nm laser (Coherent Sapphire SF 488 – 50) was cleaned up with a 488-nm notch filter, attenuated with neutral density filters, spatially filtered and expanded to ~ 2 " diameter. It was then scanned by a rotary mirror and tightly focused in the BFP of a $\times 100/1.46$ NA objective (a Plan-Apochromat, oil DIC M27, Zeiss). Images were acquired either upon evanescent-wave excitation (with the spot positioned in the extreme periphery of the objective's BFP) or upon EPI excitation (spot at 0, 0) using the laser powers and exposure times indicated. Fluorescence was collected through the same objective, filtered by a ultra flat (2-mm) long-pass 488LPXR dichroic mirror (AHF Analysentechnik), RET493LP (Semrock) and ET520LP (Chroma) long-pass filters. Band-pass filters were housed in independent filter wheels and adapted to the respective fluorophores). The filtered fluorescence was imaged on a back-illuminated sCMOS camera (PCO edge4.2bi). The effective pixel size in the sample plane was $(30 \pm 1 \text{ nm/px})$, allowing for a 3- to 4-fold binning. A Bertrand lens mounted on a motorized flipper (Thorlabs) allowed shifting the focus to the objective's BFP ($3.36 \mu\text{m/px}$ on BFP images).

SAF/UAF ratio image analysis. SP and BFP fluorescence images were subtracted with their respective dark images. BFP images were segmented into SAF and UAF regions in a multi-step process: we first found the center of the BFP pattern and the number of pixels corresponding to the limiting radius of the NA (r_{NA}). For this, we binarized the image and searched the white disk on the black background by an object recognition algorithm implemented in MATLAB. Next, we calculated the pixel radii corresponding to the critical angle of the pattern (r_c) after imposing an *a priori* RI estimate from independent measurements, $r_c = r_{NA} \times \text{RI}/\text{NA}$. Finally, we generated error bars by allowing for a positive and negative deviation (dRI) according to $r_c^{(\pm)} = r_{NA} \times (\text{RI} \pm \text{dRI})/\text{NA}$. Together, the center coordinates, r_{NA} and r_c enable us to segment the image into three areas: background, SAF and UAF. With the background subtracted, we

integrated the intensity over each area and calculate the SAF/UAF ratio $R = I_{\text{SAF}}/I_{\text{UAF}}$, where I is the respective integral over SAF and UAF areas. Repeating this integration for each dRI gave us an estimate of the dependence of SAF/UAF ratio on the accuracy of the RI estimate. For the error bars shown we opted for $dRI = \pm 0.05$.

Cell culture, staining, and microscopy. Cortical astrocytes were prepared from newborn mice, cultured and labeled previously described³⁶ (See **Supporting Experimental Procedures** for details). We systematically applied 100 μM ATP at the end of the recordings to test for cell viability and raise the intracellular Ca^{2+} . Labelling and the overall aspect of the cell culture was confirmed over a larger field on a custom upright microscope fitted for EPI and prism-type TIRF microscopy⁴⁴. FM-dye and Ca^{2+} dependent fluorescence was excited at 488- and 568-nm wavelength from a polychromatic tuneable light-source (TILL Photonics). After appropriate filtering, fluorescence was detected on a EMCCD camera (Photometrics). METAMORPH and ImageJ software were used for acquisition and image analysis. For combined TIR-SAF imaging, the same cells were transferred to the home-built inverted TIR-SAF microscope^{41, 44-46} and a tiny sub-region of the cell's footprint containing FM-loaded lysosomes imaged upon 488-nm excitation. Equipment and imaging parameters were similar to that described above.

Declarations

Acknowledgements

We thank Daniel Azulai for help with the polymer deposition, Naftali Kanovsky and Prof. Shlomo Margel for advice regarding the polymer. Thierry Bastien provided custom fine mechanics. This study was financed by the CNRS, University Paris Cité, and - mostly - by the European Union (H2020 Eureka! Eurostars, 'NanoScale', E!12848, <https://nanoscale.sppin.fr>, to MO and AS). AS acknowledges support from the French Ministry of Foreign Affairs and the French Embassy in Tel Aviv (Chateaubriand fellowship). The authors are grateful for mobility support from a Franco-Israeli CNRS-LIA, 'ImagiNano', and the FranceBio-Imaging large-scale national infrastructure initiative (FBI, ANR-10-INSB-04, Investments for the future). The Oheim lab is a member of the C'Nano Excellence Network in Nanobiophotonics (CNRS GDR2972).

Author Contributions

A.sS and M.O. developed the theory, supervised, conceived, and designed this research, wrote the paper, assembles the results, and arranged part of the figures. H.K. made the main part of the sample's fabrication, measurements, and analysis. A.S., M.O., and O.S. conceived and designed the samples analysis software and O.S, Y.A., Programmed the Image analysis tools for acquisition and analysis. All of the biological experiment's preparations, acquisitions, collection of the data, analysis, interpretations, and construction of the final figure were done at M.O.'s lab and performed by M.O. and C.J. The optical samples fabrication, characterization, and measurements were performed at A.S.'s lab. The design and composition of the microscope setup were done with the leadership of M.O and A.D. With the contribution

of I.O., H.K., O.S., and M.H. M.O. performed the simulations of the axial calibration. C.J., I.O, O.S, Y.A., A.S., M.O., collaborated and consulted about the interpretation of data and the performed analysis computations. O.S., Y.A, H.S., V.A, implemented the web platform. M.H. fabricated the plasmonic holes array and M.H, A.S. contributed to the plasmonic consultation. All authors provided critical feedback and helped in the interpretation of data, manuscript writing, and the improvement of the platform; discussed the results and contributed to the final manuscript; provided critical feedback and helped shape the research, analysis, and manuscript.

Conflict of Interest statement

There are no known conflicts of interest associated with this publication and there has been no significant financial support for this work that could have influenced its outcome.

References

1. Gleason, K. K. Nanoscale control by chemically vapour-deposited polymers. *Nat. Rev. Phys.* **2**, 347–364 (2020).
2. Leroux, Y. R. *et al.* Conducting polymer electrochemical switching as an easy means for designing active plasmonic devices. *J. Am. Chem. Soc.* **127**, 16022–16023 (2005).
3. Abad, J., Espinosa, N., García-Valverde, R., Colchero, J. & Urbina, A. The influence of uv radiation and ozone exposure on the electronic properties of poly-3-octyl-thiophene thin films. *Sol. Energy Mater. Sol. Cells* **95**, 1326–1332 (2011).
4. Loste, J., Lopez-Cuesta, J. M., Billon, L., Garay, H. & Save, M. Transparent polymer nanocomposites: an overview on their synthesis and advanced properties. *Prog. Polym. Sci.* **89**, 133–158 (2019).
5. Nagendra, B., Rizzo, P., Daniel, C., Baldino, L. & Guerra, G. C-perpendicular orientation of poly(l-lactide) films. *Polymers* **13**, 1572 (2021).
6. Nakahara, A. *et al.* Fabrication of high-aspect-ratio amorphous perfluorinated polymer structure for total internal reflection fluorescence microscopy. *Microelectron. Eng.* **88**, 1817–1820 (2011).
7. Eto, H., Franquelim, H. G., Heymann, M. & Schwille, P. Membrane-coated 3d architectures for bottom-up synthetic biology. *Soft Matter* **17**, 5456–5466 (2021).
8. Novotny, L. & Hecht, B. *Principles of nano-optics (2nd edition)*. (Cambridge University Press, 2012).
9. Cançado, L. G. & Novotny, L. Observing the angular distribution of raman scattered fields. *ACS Nano* **10**, 1722–1723 (2016).
10. Verdes, D. & Ruckstuhl, T. Supercritical angle fluorescence (saf) microscopy. *Opt. Express* **12**, 4246–4254 (2004).
11. Oheim, M., Salomon, A. & Brunstein, M. Supercritical angle fluorescence microscopy and spectroscopy. *Biophys. Perspect.* **118**, 2339–2348 (2020).
12. Ferdman, B., Weiss, L. E., Alalouf, O., Haimovich, Y. & Shechtman, Y. Ultrasensitive refractometry via supercritical angle fluorescence. *ACS Nano* **12**, 11892–11898 (2018).

13. Brunstein, M., Roy, L. & Oheim, M. Near-membrane refractometry using supercritical angle fluorescence. *Biophys. J.* **112**, 1940–1948 (2017).
14. Bourg, N. *et al.* Direct optical nanoscopy with axially localized detection. *Nat. Photonics* **9**, 587–593 (2015).
15. Niederauer, C. *et al.* Direct characterization of the evanescent field in objective-type total internal reflection fluorescence microscopy. *Opt. Express* **26**, 20492 (2018).
16. Brunstein, M., Salomon, A. & Oheim, M. Decoding the information contained in fluorophore radiation patterns. *ACS Nano* **12**, 11725–11730 (2018).
17. El Arawi, D. *et al.* Advanced quantification for single-cell adhesion by variable-angle tfrf nanoscopy. *Biophys. Rep.* **1**, 100021 (2021).
18. Liu, W. *et al.* Breaking the axial diffraction limit: a guide to axial super-resolution fluorescence microscopy. *Laser Photonics Rev.* **12**, 1700333 (2018).
19. Efremushkin, L., Sukharev, M. & Salomon, A. Molecular plasmonics: strong coupling at the low molecular density limit. *J. Phys. Chem. C* **10**, 47 (2017).
20. Oheim, M., Salomon, A., Weissman, A., Brunstein, M. & Becherer, U. Calibrating evanescent-wave penetration depths for biological tfrf microscopy. *Biophys. J.* **117**, 795–809 (2019).
21. Dai, L., Gregor, I., Von Der Hocht, I., Ruckstuhl, T. & Enderlein, J. Measuring large numerical apertures by imaging the angular distribution of radiation of fluorescing molecules. *Opt. Soc. Am.* **13**, 9409–9414 (2005).
22. El Arawi, D., Cardoso Dos Santos, M., Vézy, C. & Jaffiol, R. Incidence angle calibration for prismless total internal reflection fluorescence microscopy. *Opt. Lett.* **44**, 1710 (2019).
23. Liu, W. *et al.* Quantitative objective-based ring tfrfm system calibration through back focal plane imaging. *Opt. Lett.* **45**, 3001–3004 (2020).
24. Vézy, C., Santos, M. C. D., Déturche, R. & Jaffiol, R. Axial nanoscale localization by normalized total internal reflection fluorescence microscopy. *Opt. Lett.* **39**, 869–872 (2014).
25. Axelrod, D. Selective imaging of surface fluorescence with very high aperture microscope objectives. *J. Biomed. Opt.* **6**, 6 (2001).
26. Axelrod, D. Fluorescence excitation and imaging of single molecules near dielectric-coated and bare surfaces: a theoretical study. *J. Microsc.* **247**, 147–160 (2012).
27. Axelrod, D. & Hellen, E. H. Fluorescence emission at dielectric and metal-film interfaces. *J. Opt. Soc. Am. B* **4**, 337–350 (1987).
28. Steyer, J. A., Horstmann, H. & Almers, W. Transport, docking and exocytosis of single secretory granules in live chromaffin cells. *Nature* **388**, 474–478 (1997).
29. Oheim, M., Loerke, D., Stühmer, W. & Chow, R. H. The last few milliseconds in the life of a secretory granule. *Eur. Biophys. J.* **27**, 83–98 (1998).
30. Loerke, D., Preitz, B., Stühmer, W. & Oheim, M. Super-resolution measurements with evanescent-wave fluorescence excitation using variable beam incidence. *J. Biomed. Opt.* **5**, 23–30 (2000).

31. Li, D., Héroult, K., Oheim, M. & Ropert, N. FM dyes enter via a store-operated calcium channel and modify calcium signaling of cultured astrocytes. *Proc. Natl. Acad. Sci. U. S. A.* **106**, 21960–21965 (2009).
32. Betz, W. J., Mao, F. & Bewick, G. S. Activity-dependent fluorescent staining and destaining of living vertebrate motor nerve terminals. *J. Neurosci.* **12**, 363–375 (1992).
33. Axelrod, J. J. & Axelrod, D. Light scattering in tfr microscopy: a theoretical study of the limits to surface selectivity. *Biophys. J.* **120**, 2952–2968 (2021).
34. Szederkenyi, K., Hernandez, J. J., Attisano, L., Oheim, M. & Yip, C. M. Morphological and molecular diversity of human astrocytes in a cerebral organoid. *Biophys. J.* **121**, 153a (2022).
35. Brunstein, M., Héroult, K. & Oheim, M. Eliminating unwanted far-field excitation in objective-type tfr. part ii. combined evanescent-wave excitation and supercritical-angle fluorescence detection improves optical sectioning. *Biophys. J.* **106**, 1044–1056 (2014).
36. Kao, H. P. & Verkman, A. S. Tracking of single fluorescent particles in three dimensions: use of cylindrical optics to encode particle position. *Biophys. J.* **67**, 1291–1300 (1994).
37. Holtzer, L., Meckel, T. & Schmidt, T. Nanometric three-dimensional tracking of individual quantum dots in cells. *Appl. Phys. Lett.* **90**, 053902 (2007).
38. Watanabe, T. M., Sato, T., Gonda, K. & Higuchi, H. Three-dimensional nanometry of vesicle transport in living cells using dual-focus imaging optics. *Biochem. Biophys. Res. Commun.* **359**, 1–7 (2007).
39. Juette, M. F. & Bewersdorf, J. Three-dimensional tracking of single fluorescent particles with submillisecond temporal resolution. *Nano Lett.* **10**, 4657–4663 (2010).
40. Schütz, G. J. *et al.* 3D imaging of individual ion channels in live cells at 40nm resolution. *Single Mol.* **1**, 25–31 (2000).
41. Speidel, M., Jonáš, A. & Florin, E.-L. Three-dimensional tracking of fluorescent nanoparticles with subnanometer precision by use of off-focus imaging. *Opt. Lett.* **28**, 69–71 (2003).
42. Schnitzbauer, J., McGorty, R. & Huang, B. 4pi fluorescence detection and 3d particle localization with a single objective. *Opt. Express* **21**, 19701–19708 (2013).
43. Winckler, P., Jaffiol, R., Plain, J. & Royer, P. Nonradiative excitation fluorescence: probing volumes down to the attoliter range. *J. Phys. Chem. Lett.* **1**, 2451–2454 (2010).
44. Chen, M. *et al.* Variable-angle nanoplasmonic fluorescence microscopy: an axially resolved method for tracking the endocytic pathway. *Anal. Chem.* **91**, 13658–13664 (2019).
45. Zhai, Y.-Y. *et al.* Metallic nanofilm enhanced fluorescence cell imaging: a study of distance-dependent intensity and lifetime by optical sectioning microscopy. *J. Phys. Chem. B* **124**, 2760–2768 (2020).
46. Berndt, M., Lorenz, M., Enderlein, J. & Diez, S. Axial nanometer distances measured by fluorescence lifetime imaging microscopy. *Nano Lett.* **10**, 1497–1500 (2010).
47. Karedla, N. *et al.* Single-molecule metal-induced energy transfer (smmiet)r resolving nanometer distances at the single-molecule level. *ChemPhysChem* **15**, 705–711 (2014).

48. Ghosh, A., Chizhik, A. I., Karedla, N. & Enderlein, J. Graphene- and metal-induced energy transfer for single-molecule imaging and live-cell nanoscopy with (sub)-nanometer axial resolution. *Nat. Protoc.* **16**, 3695–3715 (2021).
49. Hwang, W. *et al.* Large field-of-view nanometer-sectioning microscopy by using metal-induced energy transfer and biexponential lifetime analysis. *Commun. Biol.* **4**, 1–7 (2021).
50. Moerland, R. J. & Hoogenboom, J. P. Subnanometer-accuracy optical distance ruler based on fluorescence quenching by transparent conductors. *Optica* **3**, 112–117 (2016).

Figures

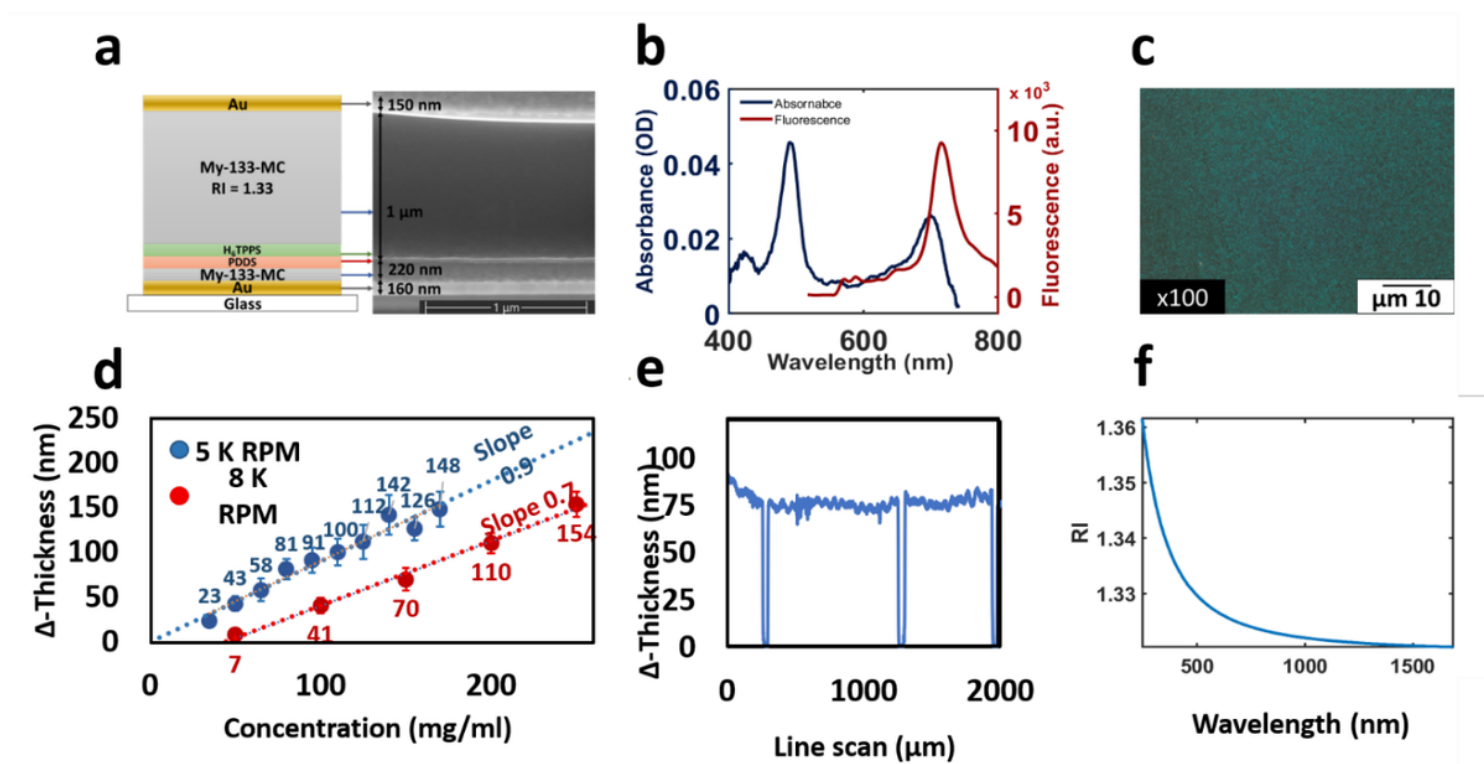


Figure 1

Multi-layered sandwich alternating transparent and fluorescent nanometric films with tightly controlled properties. (a) schematic representation (left) and measured FIB cross-section (right) of a fabricated sandwich, alternating metallic (gold), My-133-MC polymer (light blue) and dye (green) layers. Metal layers were only added for FIB imaging and normally absent. Note the thin fluorescent (4-nm) layer of H₆-TPPS J-aggregate, and the well-defined layering. (b), absorbance (blue) and fluorescence (red) spectra of TPPS films, sandwiched between polymer spacer and capping layers. (c), fluorescence micrograph of the dye layer showing a uniform surface coverage over a large scale. (d), varying the spin-coating parameters, ultra-thin layers of thicknesses down to a few nm thickness could be reproducibly produced. Thickness was measured by Stylus profilometry, (e), that equally provided a RMS roughness estimate of 1-2 nm. (f), Ellipsometry of the polymer layers revealed a RI around 1.33 in the visible range.

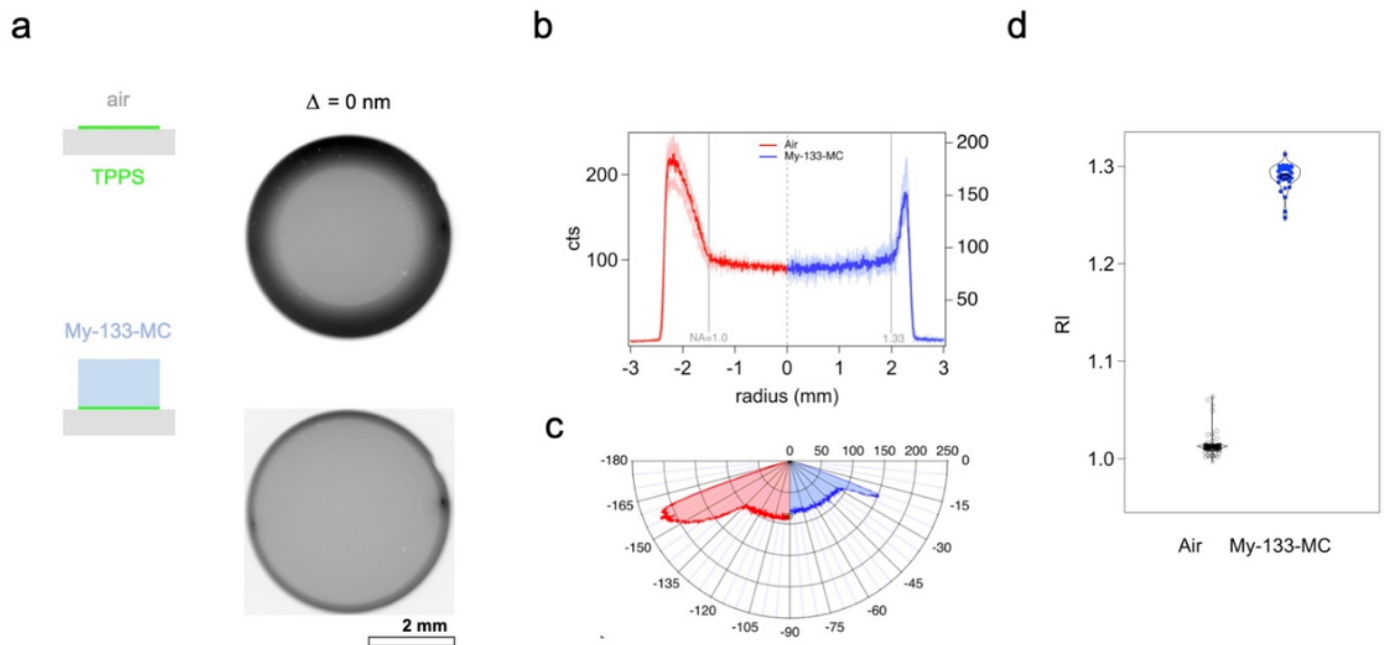


Figure 2

Supercritical-angle fluorescence (SAF)-based measurement of the refractive-index of ultra-thin transparent layers. (a) Schematic illustration of the samples (left) and BFP patterns emitted by a 5-nm TPPS J-aggregate layer (right). The dye was deposited either directly on the BK-7 substrate and left in air (top) or else covered by a 3- μm thick My-133-MC polymer capping layer (bottom). Fluorescence was excited by TIRF (see laser spots in the periphery of the pupil image). Image contrast inverted for better clarity in print. (b), vertical cross-sections of the images in (a) were largely independent of the azimuth φ . Thin, pale traces show profiles measured at $\varphi = 0^\circ, 45^\circ, 90^\circ$ and 135° , respectively. Solid darker lines are azimuthal averages that traced as polar plots in (c), revealing the characteristic directional lobes of near-interface emission at supercritical angles. Note the change in emission pattern due to the RI change from air (red) following the deposit of the polymer (blue). From the emission critical angle (grey lines in (b)), we obtained the refractive indices (RIs) of air and My-133-MC polymer, respectively, (d). Violin plots show population distributions over $n = 129$ (air) and 34 (polymer) measurements, respectively.

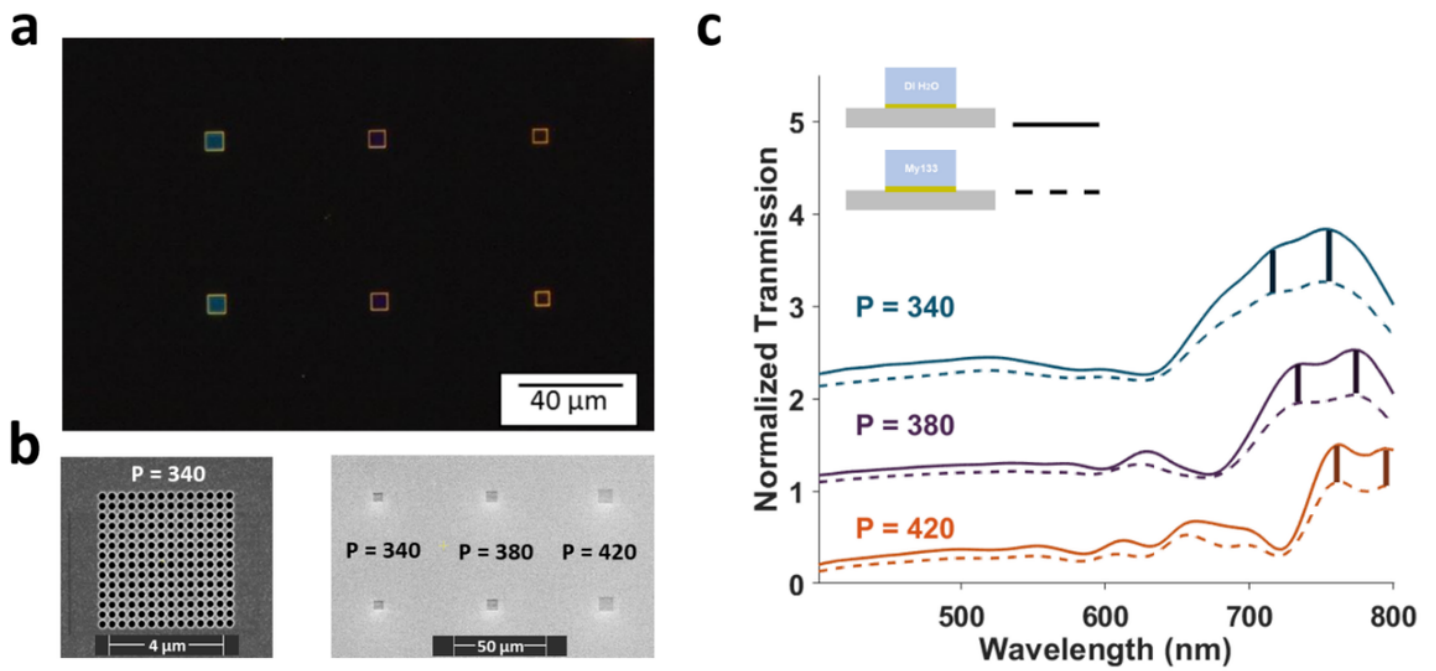


Figure 3

Thin-film RI probed on larger spatial scales. (a), dark-field image upon white-light illumination and, (b), electron micrographs of a single plasmonic hole array (left) as well as a larger plasmonic sample comprising several patterns featuring different periodicities P (in nm, right). (c), Normalized transmitted intensity vs. wavelength upon white-light illumination, showing similar responses of the plasmonic hole array when covered with water (through line) or My-133-MC polymer (dashed). Vertical lines highlight identical peak positions for the plasmonic modes at both water or My-133-MC-covered interfaces, respectively.

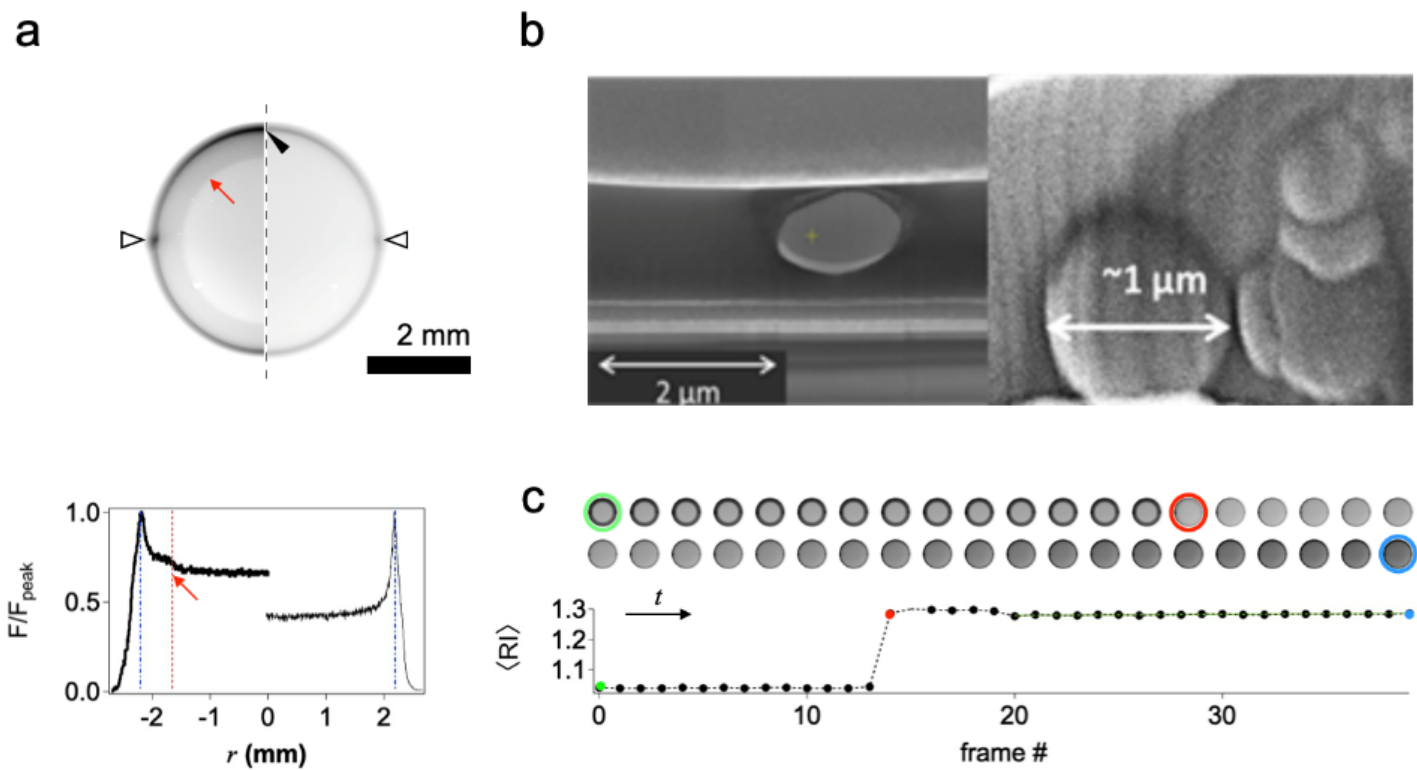


Figure 4

SAF-based detection of nano-fabrication flaws. (a), left half, example BFP image of an imperfect polymer layer displaying a double-ring structure indicative of the presence of both air (red arrow) and My-133-MC interfaces (black arrowhead). Right, typical single-ring structure observed for a flawless sample for comparison. Intensity of the left half image increased for better visibility, contrast is inverted for clarity in print, as in fig.2. Bottom, corresponding normalized-intensity line profiles. Note the kink on the left profile (red arrow), absent from the profile on the right. Dash-dotted and dotted lines indicate RI 1.33 and 1, respectively. (b), two examples of post-hoc FIB cross-sections of imperfect polymer films. (c), example of a My-133-MC polymer layer with cracks. Top, time-lapse BFP-image series and SAF-derived RI (inner ring), bottom. At frame #14, a drop of polymer was pipetted on top of the sample, increasing the measured RI from close to 1 to 1.33. Colored rings and spots, respectively, identify corresponding time frames.

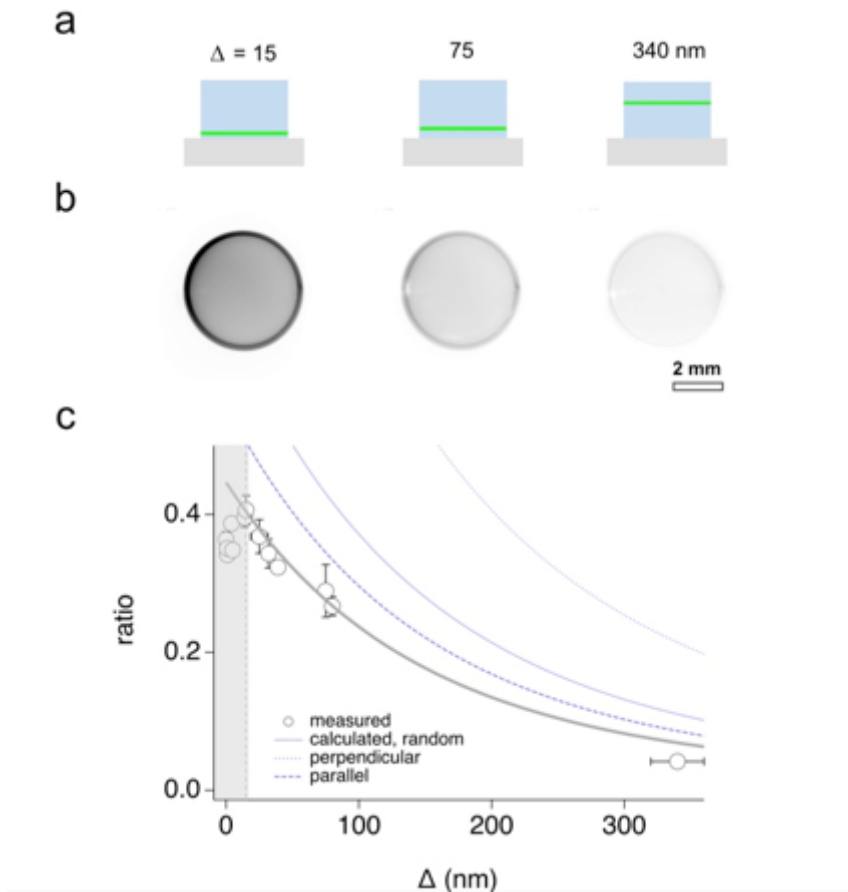


Figure 5

SAF-based axial profilometry. (a), representation of three of the prepared test slides, featuring a thin TPPS J-aggregate emitter layer sandwiched at different fluorophore heights Δ between a flat and homogenous My-133-MC spacer and capping layer. (b), measured example BFP images after background subtraction and scaled to equal min-max intensity allowing a direct comparison. (c), plot of the SAF/UAF intensity ratio R of supercritical vs. undercritical-angle fluorescence emission components vs. fluorophore height Δ . Symbols are measurements from segmented BFP images as in (b), thin blue lines are theoretical values calculated using the constant-radiated power dipole of Hellen & Axelrod (1987) for direct dipole orientations. Grey through line is the same curve as for a dipole oriented in the incidence plane, scaled to best fit and suggesting a lower collected fraction of SAF compared to UAF (seen main text). The shaded region of the first surface-proximal 15 nm was omitted from fit. Error bars were measured R_q roughness (for x) and generated (for y) by allowing for ± 0.05 RI-unit uncertainty, respectively.

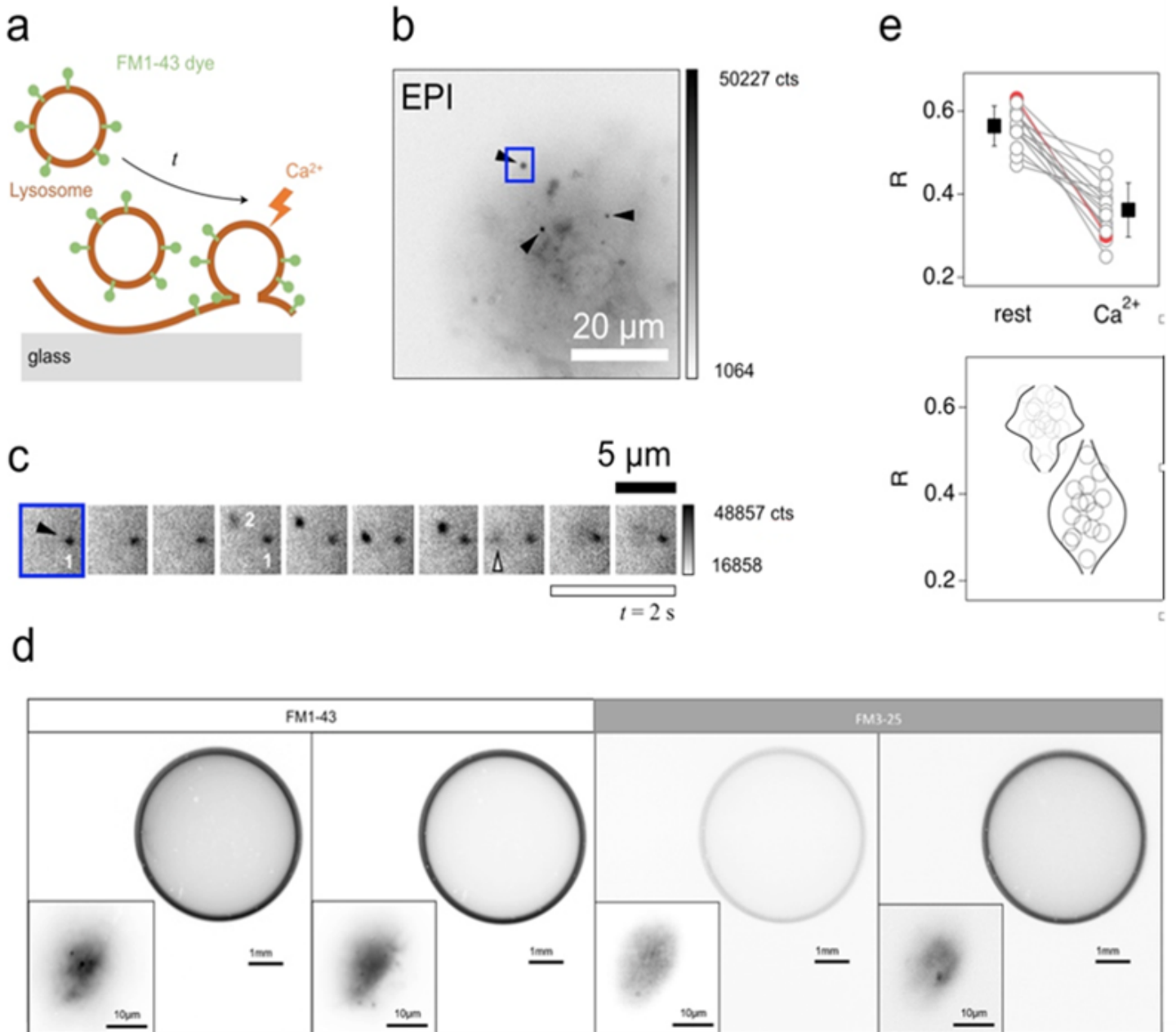


Figure 6

SAF-based disambiguation of TIRF image data. (a), schematic representation of the intracellular steps characteristic for calcium (Ca^{2+})-regulated exocytosis. FM dye (green) is a membrane-resident (brown) amphiphilic fluorophore that is internalized into cortical astrocytes and labels a tiny intracellular vesicular compartment called lysosome. These organelles approach the basal plasma membrane of cells cultured on a glass coverslip and are released in a Ca^{2+} -dependent manner (arrow). (b) epifluorescence (EPI) image showing a diffuse cytosolic labeling as well as bright spots representing individual lysosomes (arrowheads). (c), zoom on the rectangular region shown in blue on (b). The time-lapse image series acquired at 1 Hz shows two lysosomes, "1" and "2". While 2 (solid arrowhead) is present from the beginning to the end of the recording, 2 arrives in frame #3, approaches the membrane and releases its content ("exocytosis") at the moment identified by an open arrowhead. The corresponding axial re-

distribution of fluorophores is seen in (d), which examples of BFP images of ROIs (inset images) of basal membrane in cultured cortical astrocytes upon TIRF illumination, with either FM1-43 (left) or the spectrally identical but slightly more hydrophilic FM3-25 dye, right. Note the change in SAF intensity for ROIs showing membrane proximal lysosomes compared to void regions. The rightmost image is an exception because the SAF/UAF intensity ratio R dropped despite an organelle still visible, seen as a spot on the inset SP image. (e), Comparison of R values before (rest) and after (Ca^{2+}) stimulation, showing a systematic trend towards lower ratios, indicative of a loss of near-interface fluorophores consistent with exocytosis. The red trace follows the trend but corresponds to the rightmost image on d, where the lysosome apparently moved back into deeper cytoplasmic regions, thus lowering ISAF and hence R .

Supplementary Files

This is a list of supplementary files associated with this preprint. Click to download.

- [SupplementaryinformationCharacterizationnanometricfilmswithfarfieldlight.docx](#)